Supplementary Materials for

Multi-decadal patterns of fluvial morphodynamics and lahar hazard in response to episodic eruption of Soufrière Hills Volcano, Montserrat, Eastern Caribbean

James Christie*, Jenni Barclay, Georgie L Bennett, Richard Herd, Melanie J Froude, Thomas R Chudley

*Corresponding author: j.christie.ac@gmail.com
Paper DOI: 10.59236/geomorphica.v1i1.41

Table of Contents:

Supplementary Text

Summary of the Gran et al. (2011) model

A general conceptual model of fluvial evolution in response to large transient volcanic disturbances is presented by Gran and Montgomery (2005) and Gran et al. (2011). This model is derived from long term observations following the VEI 6 eruption of Mt Pinatubo, 1991. It is most relevant to eruptions which instantaneously produce $\geq 1 \times 10^9 m^3$ / 1 km^3 of sediment and cause widespread landscape modification; it is generally corroborated by findings from Mt St Helens, USA (e.g., Major et al., 2018), Santa Maria, Guatemala (Kuenzi et al., 1979), and Taupo, New Zealand (Manville et al., 2005, 2009). The model relates upstream sediment supply variability to downstream river channel morphodynamics; a schematic of sediment yields and channel evolution is shown in Figure 1.

Within the first one to two years, sediment yields may increase by multiple orders of magnitude above background rates (Figure 1, panel A) due to the presence of readily erodible pyroclastic material and flashy runoff conditions caused by infiltration-limiting fine tephra and vegetation loss. The initial process of surface tephra removal is efficient and rapid; establishment of rill and gully networks quickly follows, driving further yield increases as these networks incise and undergo headward extension. Increased flux of sediment rich in fines from upstream is delivered by large lahars which are transport-limited and tend to deposit material as the channel gradient decreases downstream. This overwhelms downstream channels, which infill and avulse, driving the formation of highly mobile river braids, and subsequently valley floor aggradation and widening (Figure 1, Panel B). Depending on the magnitude of disturbance, this initial stage may play out for a few years or up to a decade (Gran et al., 2011; Major et al., 2018).

Sediment yields subsequently decline precipitously due to upstream removal of material and stabilization of channel networks; sediment in channel margins is rendered increasingly inaccessible to flows. Vegetation recovery and removal of surface tephra also hinder runoff generation. Accordingly, sediment transport events decrease in frequency, magnitude, and sediment content; sediment delivery to downstream reaches declines; and aggradation rates wane. Sediment transport is eventually limited sufficiently to enable water flows entering lower reaches to become relatively supply limited, i.e., the supply of sediment is insufficient for them to reach carrying capacity. These relatively small flows occupy a much smaller percentage of the valley floor, and their supply limited state enables them to more readily erode the channel bed, preferentially removing fine particles (winnowing). This process encourages the formation of single threaded or anastomosing channel forms which incise into the valley floor, which can eventually result in terrace development. The removal of fines also gradually encourages armouring of the bed with larger clasts. Initially this channel incision and armouring may be seasonal, typically occurring during low flow states. Conversely, high flow states in wet seasons may deliver more sediment from upstream owing to ongoing deposit instability, thereby causing additional short-lived, seasonal aggradation. Eventually, sediment supply diminishes enough to enable year-round degradational patterns, accompanied by ecological recovery, e.g., re-establishment of aquatic life and riparian vegetation on derelict terraces/channel margins. In some cases, the degradation and recovery process is more complex, involving convoluted changes to channel cross sectional area and geometry, not simply channel bed incision and elevation change (e.g., Major et al., 2018, 2021). This aggradation to degradation cycle may play out over several decades or even centuries. Indeed, while a disturbed system will tend towards a new post-eruption equilibrium, it may never return to precisely the same pre-disturbance state (e.g., Pierson et al., 2011).

Methods

Here we provide a more detailed account of the methods used in this paper. This text refers to figures in the main text as normal, and refers to new supplementary figures as Figure S1, S2, S3… etc.

Volcanic activity and sediment supply/removal in the upper catchment

Our first objective was to produce a timeseries of the spatio-temporal distribution and estimated volume of volcanic sediment input, net volumetric change of the main deposits in the upper catchment, and a record of morphological changes occurring on these deposits. Most of the compilation of recorded volcanic activity and valley fill analysis was completed by Froude (2015) via consultation of MVO records, published literature (e.g., Cole et al., 1998, 2002; Calder et al., 2002; Sparks et al., 2002, Herd et al., 2005, de Angelis et al., 2007, Alexander et al., 2010, Cole et al., 2014, Stinton et al., 2014a, b) and aerial photography-derived estimation of valley fill. We have complemented this record by estimating the quantity of sediment within relevant sub-catchments via Digital Surface Model (DSM) difference analysis, for which we have created a new volcano-wide DSM (see below). Table S1 lists the Digital Surface/Elevation Models (DSM/DEM) used in this paper.

We generated a new volcano-wide photogrammetry-derived DSM via processing of very high resolution (0.5 m) Pleiades tri-stereo satellite imagery acquired as part of the Committee of Earth Observing Satellites (CEOS) landslide hazard data access pilot scheme. Photogrammetry is a means of generating 3-dimensional renderings of physical objects with a series of overlapping 2-dimensional optical images (e.g., Westoby et al., 2012; Mancini and Salvini, 2019). Satellite photogrammetry requires pairs, or in this case, triplets, of overlapping images acquired at different along-orbit positions (Figure S1a). It is dependent on the known location of the acquisition sensor in 3-D space (a.k.a. ephemeris), determined by GPS, and its attitude, i.e., its orientation (pitch/roll/yaw), with respect to the Earth's surface (e.g., Stumpf et al., 2017; Hodúl et al., 2018). These characteristics are then used to define a Rational Function Model (RFM) which makes use of a series of Rational Polynomial Coefficients. The RFM can triangulate features by identifying lines/samples common to overlapping sets of images, measuring spatial differences between them, and converting to object space, i.e. XYZ coordinates, thereby generating a 3-D model. Errors in the measurement of ephemeris and attitude can lead to subsequent synoptic horizontal and vertical errors in resulting DSMs. These errors are typically translational and consistent across a scene and may be corrected via georeferencing and/or co-registration techniques (e.g., Akca et al., 2010; Stumpf et al., 2017; Hodúl et al., 2018). Importantly, this method returns a Digital Surface Model, not a Digital Elevation Model, as optical imagery includes vegetation and other features which obscure the land surface. It is important to acknowledge this key difference between DEMs and DSMs: DSMs are a model of the land surface, including any overlying vegetation or features; by contrast, DEMs are a model of the land surface without any overlying features. The difference is usually due to the method of generation. For example, models derived from optical imagery include vegetation and buildings. Conversely, LiDAR/radar techniques and use of GPS may penetrate vegetation cover and more accurately capture the land surface.

As part of the CEOS scheme, we received a triplet of panchromatic images with a resolution of 0.5 m; 3 m resolution multi-spectral images were also provided. We processed the raw panchromatic imagery to generate a DSM using the European Space Agency Geohazards Exploitation Platform (ESA GEP) DSM-OPT software, hosted by Terradue (Stumpf et al., 2017). This platform is mostly black-box in that, following imagery upload, RFM processing and DSM construction are automated aside from a user-defined resolution parameter with a minimum value of 0.5 m. We set this resolution as 1 m in keeping with the resolution of the 2010 LiDAR DSM. This returned a high-resolution DSM of the south of the island which was displaced in the X, Y and Z domains by approximately 20 m with respect to the June 2010 LiDAR DSM; co-registration was therefore required.

Co-registration of DSMs involves matching a new surface model to a reference surface model; in other words, the new model is relocated in space to best fit the reference model (Akca et al., 2010; Bertin et al., 2022). Owing to software access limitations, we used the trial version of the Least Squares 3D (LS3D) surface matching software (Akca et al., 2010). This software package has a limited memory capacity and was unable to process the co-registration of the entire new DSM. To address this memory limitation, we fragmented the new and reference DSMs into a series of much smaller sections (~3-4 km^2). Via trial and error, we created 7 pairs of rectangular extractions of both new/reference DSMs which we then processed individually with the LS3D software. 7 co-registered versions of the fragments of the new DSM were returned, which we then merged into one raster covering the volcanic deposits in the upper catchment and the main Belham Valley channel (Figure S1b). This excludes 1) portions of the surrounding Centre Hills as no significant deposition/erosion has occurred here, 2) the coast because DSMs including the coast caused LS3D to malfunction (the reason for this is unclear but may be a function of the noise in the DSM over the sea), and 3) the summit of the volcano because the 2010 LiDAR DSM also did not cover the summit due to cloud cover.

Together with the co-registered DSM, LS3D produces files of vertical residuals; we calculated the root mean square error (RMSE) from these residuals which returned RMSE = 2.7 m. Understanding that these residuals included geomorphic changes, changes in vegetation cover, and growth of pre-existing vegetation, we manually selected stable benchmarks from across the catchment (large boulders, buildings) identifiable in both DSMs to constrain a new RMSE of 2.3m. This error is high compared to some other DSMs used in this study (Table S1), and higher than other DSMs in volcanic settings generated with Pleiades data e.g., <0.8 m (Bisson et al., 2021) and 1.8m (Walk et al., 2019). However, these examples were both generated for surfaces with little or no vegetation or anthropogenic structures; therefore, they are not affected by overlying surface changes in the same way. Thus, a higher error is expected in our case and not unreasonable given the vegetated surfaces included in the new 2019 DSM. We argue that in light of the challenges outlined above this constitutes a success; indeed, two of the DSMs used in this study have higher errors than this (pre-eruption and 1999 DSMs have an error of 5 m).

DSM/DEM differencing enables the quantification of land surface change and is used commonly in volcanic contexts (e.g., Major et al., 2018; Dai et al., 2022; Lillo et al., 2024; Sutton et al., 2024; Vallejo et al., 2024). For our analysis, we used the ESRI ArcMap plugin, '*Geomorphic Change Detection*' ('*GCD*'), developed by Wheaton et al. (2010). GCD incorporates user-defined vertical errors of each of the compared DSMs into its calculations of geomorphic change and automatically generates error bounds which inform a Minimum Level of Detection (LoD). The LoD thus enables the masking of apparent geomorphic change that may be due to error. The catchment-wide DSMs from pre-1995, 1999, 2010 and 2019 (Table S1) were processed in GCD to elucidate the net changes in the upper catchment over the periods pre-1995 – 1999, 1999 – 2010, 2010 – 2019, and the overall change between pre-1995 – 2019. Other channel-limited DEMs listed in Table S1 contribute to the analysis of channel change in the Middle and Lower Belham (see more below); differencing was conducted in the same way.

Topographic change can induce migration of watershed boundaries (e.g., Gran and Montgomery, 2005), thereby increasing or decreasing watershed size. This has a knock-on effect on the quantity of rainfall incident within a catchment boundary, the quantity of water available for runoff, and thus the potential discharge and sediment transport capacity of flows; this is therefore an important consideration. Watershed delineation requires analysis of catchment-scale, or larger, DSMs. Here, we have been able to extract the watershed areas for pre-1995, 1999 and 2010 in ESRI ArcMap using the Watershed tool.

DSM differencing between 2010 and 2019 permits measurement of the *net* erosion of pyroclastic deposits between these dates. However, constraining the *rate* of this erosion is of interest. With the use of high-resolution RapidEye (3 m resolution) and Pleiades (0.5 m resolution) satellite data (Table S2), we measured lateral erosion of channel margins at 20 evenly spaced transects along a 650 m section of Dyer's River (upstream and downstream of D2, Figure 4) from 2010-2011, 2011-2014, 2014-2019, to establish relative rates of erosion in the upper catchment (e.g. Waythomas et al., 2010). We selected this reach owing to its relative straightness and simpler channel morphology compared to upper Dyer's River and Tyer's Ghaut. We have rationed the net erosion (as calculated by GCD) proportionately between these time periods according to measured rates of lateral erosion to establish variation in total erosion rate. In doing this we assume that 1) lateral erosion has occurred proportionally with vertical erosion in this reach and is therefore an adequate proxy of total erosion; and 2) erosion in this reach is proportional to erosion in other parts of the upper catchment. Whether these assumptions are realistic is uncertain, as factors controlling the rate of channel widening and incision are complex (e.g., Finnegan et al., 2005).

With this new analysis, combined with the catalogue of activity and geomorphic changes compiled by Froude (2015), we have rationed estimates of sediment deposition per day on which deposition was recorded. We have therefore been able to produce:

1) a timeseries of the estimated *average* deposition for each day on which pyroclastic flows were recorded entering Tyer's Ghaut and the North Gage's Fan (data is more limited for the latter).
2) a timeseries of the estimated volume of sediment removed, i.e., sediment yield, from upper catchment by erosion.

In both cases, our estimation is mostly limited to Tyer's Ghaut owing to a lack of data elsewhere.

Vegetation

Due to its importance in mediating the rainfall-runoff response following volcanic disturbance (e.g., Alexander et al., 2010; Pierson and Major, 2014), our next consideration was the spatio-temporal variation of vegetation cover throughout the study period. Observations of vegetation cover over the whole catchment are limited in photographic archives and in the literature, e.g., Alexander et al. (2010) provide estimates between May and November 2006. Fortunately, island-wide aerial photography acquired in February 1999 is available, and multi-spectral satellite imagery is available on a quasi-annual basis from 2001 onwards.

Leaves and other chlorophyll-laden parts of plants absorb red light for photosynthesis and reflect infrared light to mitigate thermal tissue damage. Observing the difference between the reflectance of these two bands of light provides an indication of the intensity of photosynthesis within a pixel, and thus can be used as a proxy measure of plant health. The Normalised Difference Vegetation Index (NDVI) is a commonly used proxy measure of photosynthetic activity on a land surface and has been previously used to detect vegetation impacts of landscape disturbances (as detailed in the main body of text).

Satellite images used in this study have come from various sensors, shown in Table S2. Satellite images need to be processed to different degrees depending on the type and nature of available data prior to being used for analytic purposes. NDVI analysis requires surface reflectance data and for clouds/cloud shadows to be masked/removed from the image; in NDVI clouds can be mistaken for bare surface (e.g., Buma, 2012; Lai et al., 2022; Lindsay et al., 2022). Cloud cover is very common in Montserrat, particularly over the volcano summit and parts of the Upper Catchment. This reduces data availability, a problem common to many tropical regions (Hall et al., 2012, Chandra et al., 2019). We chose images to ensure at least 75% of the images were cloud-free and, where possible (i.e., with LandSat-7 data), temporal median composites were developed to mitigate data loss (e.g., Yan and Roy 2014; Shelestov et al., 2017; Lindsay et al., 2022). We paid due consideration of the dates of known vegetation disturbances (e.g. large eruptive events) to avoid mixed signal across composite images. The latter was unfortunately not possible in 2001; this composite image may contain some mixed signal owing to impacts from transient tephra fall associated with a dome collapse (Carn et al., 2004). LandSat-7 data acquired for this work was fully processed automatically through Google Earth Engine, which returned cloud-masked (i.e., cloud pixels removed) surface reflectance (i.e., atmospheric correction applied) data which was then composited to further reduce data loss from cloud cover. Data from ASTER (Level 2), Pleiades, RapidEye, and PlanetScope were delivered as surface reflectance data but required manual cloud masking using supervised classification on ESRI ArcMap.

Cloud masking is the removal of cloud pixels from images. This is important for analytical purposes owing to the spectral response of clouds; in NDVI analysis, clouds return low NDVI values which are not representative of the land surface beneath the cloud. Clouds therefore must be removed to avoid cloud-induced bias in the measurements. Thus, once all the data was in an appropriate format, with exception of LandSat-7 data, all available constituent bands for each sensor were merged into a single mosaic raster and then cloud masked using the Supervised Maximum Likelihood classification tool within ESRI ArcMap. Clouds have a different spectral response compared to both vegetated and bare land surfaces across the Visible (V), Near Infrared (NIR), short wave infrared (SWIR), and thermal infrared (TIR) bands (Chandra et al., 2019). Merging into a single mosaic multi-band raster enables the classification tool to classify according to the variance of pixel values across all bands, rather than considering bands individually.

Supervised classification requires the provision of manually selected training data which is created via delineation of areas containing pixels that are representative of different classes of landcover types (i.e., volcanic deposit vs vegetation), sea, or clouds. Table S3 shows the classes of landcover types we designated for this analysis and whether a mask was applied to them to remove them from the image. We selected these classes based on the types of features/landcover I could identify in the optical imagery. To select training data, we manually drew polygons over an RGB image which enveloped only features belonging to each respective class. Once classified, the multi-band mosaic rasters were masked, eliminating any pixels contaminated by cloud or cloud shadow (as per Table S3). We then isolated the Red and NIR bands from the masked mosaic rasters, before running them through the NDVI function within ArcMap.

Once classified, clouds pixels were removed, and we could then perform NDVI analysis on these images. NDVI analysis returns values from -1 to 1; the highest values indicate higher photosynthesis. Following Rodgers et al. (2009), we identify land surface cover of three main types: Type 1 = bare surface/severe vegetation damage; Type 2 = thin - moderate density vegetation (grassland/scrubland); Type 3 = high density vegetation (i.e., including low-lying but dense greenery, to full forest). Here, we are particularly interested in the balance between bare surface/severe damage, and any vegetated surface, so adopt a ratio of Type 1 to Type 2+3. Rodgers et al. (2009) adopt threshold values for these land cover types, namely, Type 1 = NDVI <0.2, Type 2 = NDVI 0.2-0.6, Type 3 = NDVI >0.6. However, in their case, data was sourced from one sensor (LandSat); we have used multiple. Note in Table S2 the range of red and NIR bands for each sensor varies; any resultant NDVI values will also vary.

To help ensure as accurate an assessment of vegetation cover as possible via NDVI, these images required calibration with ground observations; this was a challenge. The most sophisticated validation methods involve the comparison of satellite NDVI values with NDVI values obtained by multispectral aerial or UAV imagery (e.g., Sotille et al., 2020; Tang et al., 2020; Thapa et al., 2021), which was not possible in our case. Alternatively, ground truthing and validation/verification of NDVI findings have been performed with use of ground/aerial photography (e.g., Rivas-Torres et al., 2018, Valderrama-Landeros et al., 2018). We have been able to perform a limited calibration process using photography available from the MVO archive taken from known and identifiable locations at various dates that are congruent with satellite image acquisition dates. Figure 6 shows the resultant NDVI value ranges for each land surface type for each sensor.

In line with the outlined land surface types (Types 1, 2 and 3, identified above) we have first identified areas of bare surface (i.e., deposit) or dense vegetation in aerial photographs taken at various times throughout the study period and are temporally congruent with satellite imagery from the 5 satellite sources (i.e., ASTER, LandSat-7, RapidEye, Pleiades, and PlanetScope). Areas of thinner vegetation have been more variable owing to spatiotemporal variability of volcanic impacts, so finding areas common across both aerial and satellite images was generally more challenging; this said, open spaces, e.g., sports fields and large residential gardens, have remained relatively constant throughout. We have then examined the associated NDVI values by taking >100 randomly selected point samples over the identified areas for each surface type. Thus, we have a range of NDVI values for each of the 3 land cover types (i.e., Types 1, 2 and 3) for the 5 sensors. These are shown in Figure S2; there is clearly variance between the NDVI values measured by each sensor for each land cover type. This may be an artifact of both variable plant health between imagery dates (e.g., impact of seasonal changes) and variable wavelength bands detected by the sensors (as shown in Table S2). It is clear that the 0.2 threshold from Rodgers et al. (2009) is appropriate for LandSat and ASTER, but not in the other cases. Instead, by comparing maximum/minimum values of each sample population (excluding outliers), we have established thresholds for each land cover type for each sensor, shown by horizontal dotted lines in Figure S2.

Finally, the February 1999 aerial photography covered the entire south of the island; some of this imagery was used to generate the 1999 DSM (Wadge, 2000). It consists of a series of images that form an overlapping mosaic; four of these images cover the BRV. We georeferenced the four relevant images using ArcGIS Pro using buildings identifiable in the 2010 DSM as benchmarks, then merged the images into one raster file. The resulting image had a spatial resolution of 0.73 m. Happily, the image was cloud free, so no cloud masking was required prior to classification of land-cover types. The image was classified using Maximum Likelihood Supervised Classification native to ESRI ArcMap and areal extents were estimated for each landcover type.

Lahars and geomorphic change

The Belham River is not monitored specifically (e.g., with stream gauge, force plate, near-field seismometers). Instead, records of lahars are based upon observations made in the valley (direct observations of flows and/or deposits) and detection by far-field seismometers/helicorders installed around the island for the purposes of volcano monitoring. Lahars generate a distinct seismic signal (longer in duration, distinct frequency range) compared with other volcanic phenomena (PDCs, rockfalls, VT earthquakes) which allows their identification (Zobin, 2022; Froude, 2015; Johnson et al., 2023). The lack of direct monitoring of the valley necessitates a crude definition of lahar magnitude: small, medium, or large, based on a series of criteria set out by Froude (2015) as shown in Table S4. Froude (2015) compiled a record of lahars between 1995 – 2013; we have added to this record by consulting MVO activity logs and multiband seismic records between 2013 - 2023 (seismometer locations shown in Figure 7). For reference, simulations run by Darnell et al. (2012) suggest plausible volume estimates by size also shown in Table S4. Some inconsistency exists between the volume estimations provided by Froude (2015) and Darnell et al. (2012). For example, Darnell et al. (2012) assert that to reach the sea, a lahar would exceed 1 x 10^5 m^3 (i.e., large), whereas for Froude (2015), and here, reaching the coast is a criterion for designating a medium lahar.

Geomorphic changes in the Middle and Lower Belham, resulting from lahar activity and the occasional long runout PDC, have been captured in a catalogue of ground-based, aerial, and satellite photography, periodic DEM surveys (e.g., Tables S1 and S2), and documented in several literature sources (Barclay et al., 2007; Susnik, 2008; Alexander et al., 2010; Darnell, 2010; Froude, 2015; Froude et al., 2017). This record provides both quantitative and qualitative snapshots of the conditions in the valley, capturing the net changes in the channel over elapsed spans of time. High resolution aerial imagery of the whole catchment is also available from February 1999. With this imagery we estimated channel/valley fill volume by establishing a filled channel width at 30 transects along the middle and lower reaches (4 km). By extracting topographic cross-sections from the pre-eruption DSM at each transect, we calculated the cross-sectional area of the filled channel (Figure S3). We have taken the mean of these cross-sectional areas and multiplied by the length of the middle and lower reaches to gain an approximate volume. The error of this calculation is very high owing to the large vertical error of the pre-eruption DSM (+/- 5 m); in some places this error exceeds the likely depth of deposit.

We have compiled a record of changes along the coastline at the mouth of the Belham Valley using satellite and aerial photography. It was possible to crudely estimate the volume of the coastal fan either by using ground-based photography by comparing the height of deposit surface with respect to an old jetty, (~1.5m above sea level at the pre-eruption mouth of the Belham River; Froude, 2015), or by point sampling DSMs of the fan where possible. No data are available concerning the sub-marine portion of the fan, other than the ~10 m depth of the pre-eruption harbour (Froude, 2015), so our estimates only apply to the sub-aerial portion of the fan and up to this 10 m depth.

By combining data derived from both, 1) the estimates of erosion within the upper catchment, and 2) estimates of deposition in the middle and lower reaches, we have produced a timeseries of the estimated specific sediment yield (SSY) from the Upper Catchment (area of 6.4 km^2). Specific sediment yield is a commonly adopted metric of sediment yield normalised by catchment area and time, with units m^3 km^{-2} yr^{-1}, which enables comparison with other fluvial systems (e.g., Lavigne, 2004; Burt and Allison, 2010; Waythomas et al., 2010; Gran et al., 2011; Thouret et al., 2014). Our estimates are strictly minimum estimates because it has not been possible to perform a complete sediment budget analysis for this catchment. Firstly, measurements of the upper catchment are relatively sparse and predominantly limited to Tyer's Ghaut (most exclude Farrell's Plain, Dyer's River and Gage's Fan). Secondly, we are unable to account for sediment deposition at sea, which is likely to be significant (e.g., Le Friant et al., 2010; Karstens et al., 2013).

Supplementary Figures

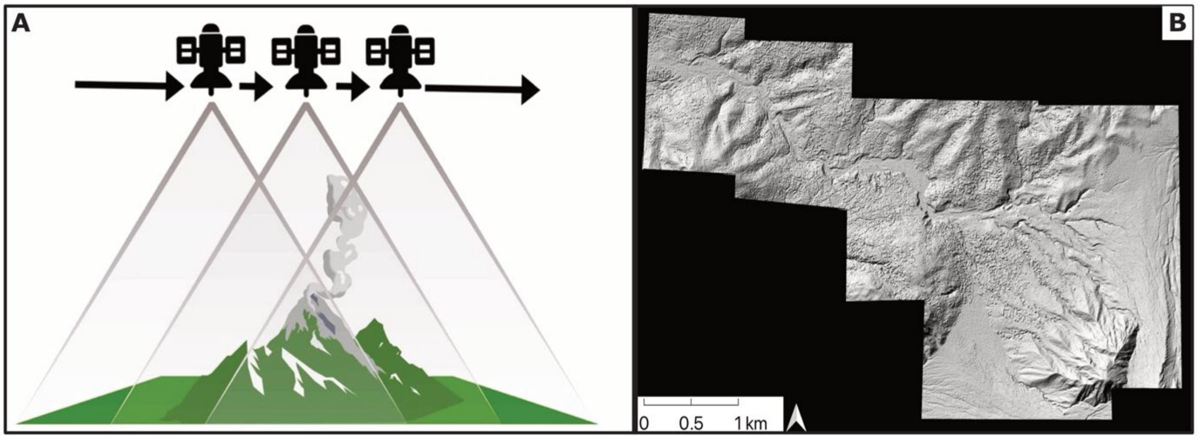

Figure S1. (a) Schematic of tri-stereo imagery capture. (b) Hillshade render of the resultant co-registered DSM from 2019.

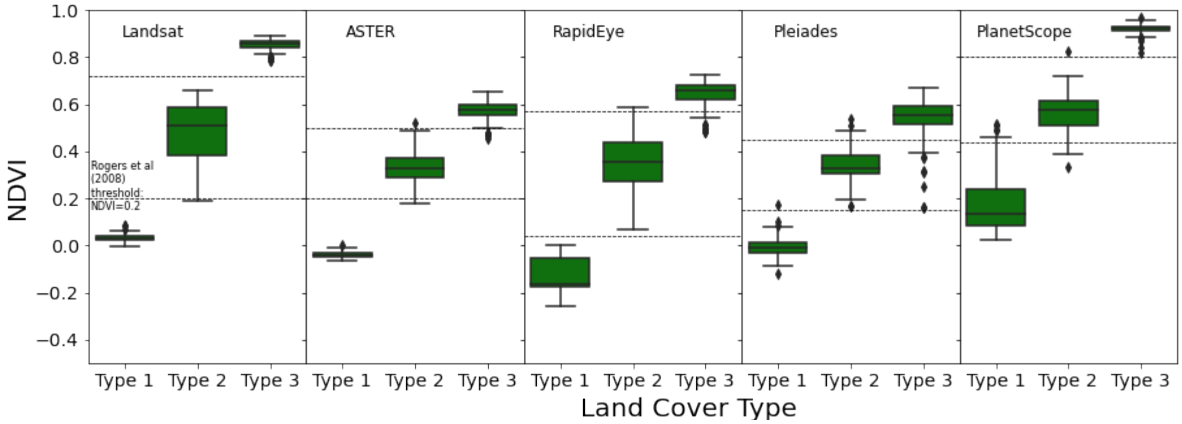

Figure S2. Boxplots of sampled NDVI values for each land cover type and for each sensor. Dotted lines indicate thresholds adopted based on comparison of minimum/maximum values for each sample population.

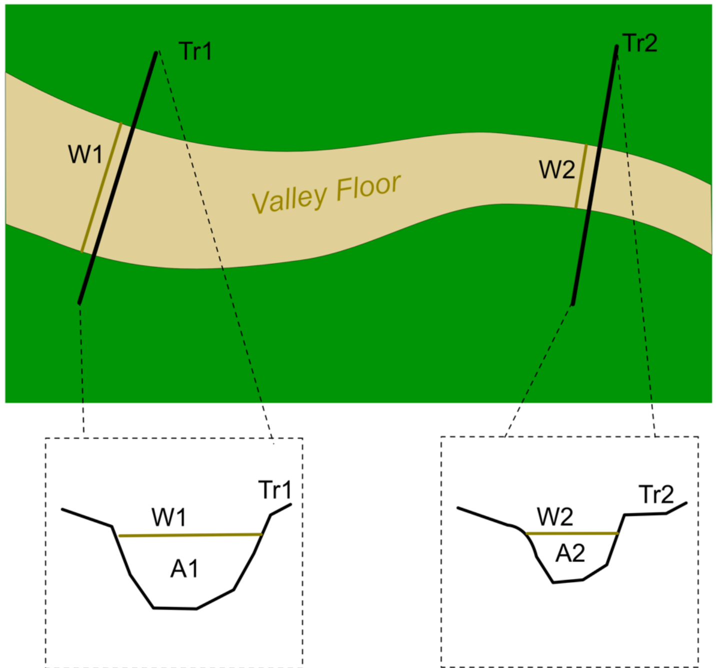

Figure S3. Schematic of approach used to estimate valley fill volume from measured valley floor width from 1999 aerial photography. Tr = Transect; W = Valley Width; A = Cross Sectional Area.

Supplementary Tables

Table S1. List of digital surface models used in the analysis of this paper.

Date	Source	Spatial resolution (m)	Vertical error (m)	Extent
Pre eruption	Digitised contour map	10	5	DSM: Whole island (Wadge and Isaacs, 1988; MVO)
Feb 1999	Aerial Photogrammetry	10	5	DSM: Whole island (Wadge, 2000; MVO)
Jan 2002	GPS survey (Leica AT302)	10	0.01-0.02	DEM: Channel-limited from 1.4km upstream of coast, extending 610m (MVO/NERC)
May 2003	GPS survey (Leica AT302)	10	0.01-0.02	DEM: Channel-limited from 1.4km upstream of coast, extending 930m (MVO/NERC)
May 2005	GPS survey (Leica AT302)	10	0.01-0.02	DEM: Channel-limited coast to Sappit River (Susnik, 2008)
Nov 2006	GPS survey (Leica AT302)	10	0.01-0.02	DEM: Channel-limited coast to Lee's Channel (Darnell, 2010)
Nov 2007	GPS survey (Leica AT302)	10	0.01-0.02	DEM: Channel-limited coast to Lee's Channel (Darnell, 2010)
Jun 2010	LiDAR DSM	1	0.15	DSM: Volcano-wide (MVO)
Mar 2011	GPS survey (Leica AT302)	10	0.01-0.02	DEM: Channel-limited coast to Lee's Channel (Froude, 2015)
Mar 2012	GPS survey (Viva GNSS GS15)	10	0.035	DEM: Channel-limited coast to Lee's Channel (Froude, 2015)
Mar 2013	GPS survey (Viva GNSS GS15)	10	0.035	DEM: Channel-limited coast to Lee's Channel (Froude, 2015)
Mar 2019	Tri-stereo Satellite Photogrammetry	0.5	2.3	DSM: Majority of Belham catchment, excludes coast.

Table S2. Data sources, relevant statistics and acquisition dates of synoptic aerial/satellite imagery used during this study. 'C' indicates median composite image over the time span indicated. *Not used for vegetation analysis.

Sensor	**Available bands**	**Red (nm)**	**Infrared (nm)**	**Resolution (m)**	**Acquisition Date**
Aerial Photography (Wadge 2000; supplied by MVO)	-	-	-	0.73	Feb 1999
ASTER	V/NIR = 3 (Until 2008) SWIR = 4	630 – 690	760 – 860	15	13 Apr 2002 14 Sep 2003 21 Feb 2010
Landsat-7	V/NIR = 4 SWIR = 2 TIR = 1	630 – 690	770 – 900	30	Jan - Dec 2001 C Jan - Dec 2004 C Jan - Mar 2006 C Jan - Jun 2007 C Jan - Sep 2008 C Feb - May 2009 C
Quickbird*	V/NIR = 4	630 – 690	760 – 900	2.4	26 Jun 2006 18 Nov 2007
RapidEye	V/NIR = 5	630 – 685	760 – 850	5	09 Apr 2011 14 Feb 2012 07 Jan 2014
Pleiades (provided by CEOS)	V/NIR = 4	600 – 720	750 – 950	0.5	11 Apr 2014 06 Apr 2017 30 Jan 2018 29 Mar 2019
PlanetScope	V/NIR = 4	590 – 670	780 – 860	3	07 Oct 2020 13 Feb 2021 06 Feb 2024

Table S3. Details of classes defined in the image classification process and masking status.

Class	Description	Mask
Vegetation (Forest)	Forested land surface	NO
Vegetation (Thin)	Land surface vegetated by non-forest vegetation	NO
Vegetation (Damage)	Land surface covered by damaged vegetation (discoloured)	NO
Vegetation (Cloud Shadow)	Any vegetated surface shadowed by cloud	YES
Deposit	Bare volcanic deposit	NO
Deposit (Bright)	Bare volcanic deposit that appears unusually bright compared to surrounding deposit	NO
Deposit (Cloud Shadow)	Any deposit shadowed by cloud	YES
Cloud	Cloud tops	YES
Cloud edge (Vegetation)	Any cloud edge above a vegetated land surface	YES
Cloud edge (Deposit)	Any cloud edge above a volcanic deposit	YES
Sea	Any part of the image that contains the sea.	YES

Table S4. Categorisation of lahar magnitudes used in this study as set out by Froude (2015). Reference volumes from LAHARZ modelling simulations by Darnell et al. (2012) are also shown.

Size	**Froude (2015)**	**Darnell et al. (2012)** reference volumes from LAHARZ simulations
Small	Duration: Tens of minutes to a few hours. Extent: Limited to small percentage of valley floor at B4. Does not reach the sea.	~0.5 x10^4 m^3 (small)
Medium	Duration: May have multiple pulses over a few hours up to and exceeding 12 hours. Extent: Limited to ~50% of valley floor at B4. Reaches the sea.	~2.5-5.0 x10^4 m^3 (medium)
Large	Duration: Multiple pulses over a period lasting up to and exceeding 24 hours. Extent: Occupies entire valley floor at B4. Reaches the sea.	~1.0 x10^5 m^3 (large) and ~1.0 x10^6 m^3 (extreme).

Table S5. This table is too large for this document and can be found at the following DOI: 10.5281/zenodo.15036159.

Table S6. List of the most significant sediment supply events in the BRV.

Date/Date Range	**Estimated Volume ($x10^6$ m^3)**	**Source**	**Note**
Jun 1997 – Oct 1998	22	Cole et al., 1998; Norton et al., 2002; This Study	Intra- and inter-phase dome degradation/ collapse
Late 2001 – Jul 2003	4.2	Wadge et al., 2014; This Study	Continual shedding of the dome to north and west.
15th Jul 2003	0.9	Herd et al., 2005; Edmonds et al., 2006	Significant tephra fall from major dome collapse
8th Jan 2007	4.5	De Angelis et al., 2007	Major PDC; long runout, reaching B3
2nd Jan 2009	0.5	Wadge et al., 2014	PDC
8th Jan 2010	3.4	Stinton et al., 2014a	PDC
11th Feb 2010	1.3	Stinton et al., 2014b	PDC associated with partial dome collapse.

Table S7. Tabulated net deposition/erosion derived from Geomorphic Change Detection for each reach over survey periods. Units are x$10^6$$m^3$. +/- values are GCD-propagated error from DSM errors. Bold indicates measures of net change from catchment-wide DSMs. Italic and grey highlight indicates erosion. '-' indicates no data, 'FP' = Farrell's Plain. Note: the DEMs from 2002, 2003 and 2005 were limited to small portions of the Lower Belham (see Table S1) and are thus indicative only of local changes.

Reach	Tyer's/FP	Hussey	N. Gage's	Dyer's	Middle Belham	Lower Belham	All
Jul 1995 – Feb 1999	**8.2 +/- 3.7**	**-**	**13.6 +/- 4.0**	**-**	**-**	**-**	**22.0 +/- 7.9**
Jul 1995 – Jan 2002	-	-	-	-	-	0.68 +/- 0.07	-
Jan 2002 – May 2003	-	-	-	-	-	0.06 +/- 0.01	-
May 2003 – May 2005	-	-	-	-	-	*-0.008 +/- 0.005*	-
May 2005 – Nov 2006	-	-	-	-	-	0.51 +/- 0.06	-
Nov 2006 – Nov 2007	-	-	-	-	0.83 +/- 0.07	0.3 +/- 0.2	-
Nov 2007 – Jun 2010	-	-	-	-	0.50 +/- 0.03	0.13 +/- 0.07	
Feb 1999 – Jun 2010	**2.2 +/- 1.5**	**-**	**4.7 +/- 2.1**	**1.6 +/- 0.6**	**2.1 +/- 0.7**	**1.1 +/- 0.7**	**12.0 +/- 5.7**
Jun 2010 – Mar 2011	-	-	-	-	0.06 +/- 0.05	0.53 +/- 0.05	-
Mar 2011 – Mar 2012	-	-	-	-	*-0.02 +/- 0.03*	*-0.10 +/- 0.03*	-
Mar 2012 – Mar 2013	-	-	-	-	*-0.02 +/- 0.03*	*-0.02 +/- 0.01*	-
Mar 2013 – Mar 2019	-	-	-	-	*-0.3 +/- 0.1*	*-0.6 +/- 0.3*	-
Jun 2010 – Mar 2019	***-0.3 +/- 0.2***	***-0.16 +/- 0.08***	***-0.12 +/- 0.06***	***-0.6 +/- 0.2***	***-0.2 +/- 0.1***	***-0.6 +/- 0.3***	***-2.0 +/-0.9***
Jul 1995 – Mar 2019	**10.6 +/- 2.7**	**-**	**9.5 +/- 3.1**	**1.0 +/- 0.5**	**1.8 +/- 0.9**	**0.3 +/- 0.2**	**23.3 +/- 7.4**

Table S8 List of key periods of incision observed within Tyer’s Ghaut and Dyer’s River and approximate volume of sediment removed by this incision if known. ‘Qualitative’ indicates that channel incision was observed, but quantification was not possible.

Date Range	**Estimated Volume ($x10^6$ m^3)**	**Source**
Oct 1998 – Feb 1999	0.84 ± 0.03	Froude (2015)
Feb 1999 – Jan 2002	0.29 ± 0.03	Froude (2015)
Jul 2003 – Jun 2005	2.28 ± 0.03	Froude (2015)
Jun 2005 – Nov 2006	0.58 ± 0.03	Froude (2015)
Jan 2007 – Dec 2008	[qualitative]	Froude (2015)
Feb 2010 – Mar 2019	1.1 ± 0.5	This study
Mar 2019 – Jan 2024	[qualitative]	This study

Table S9. Frequency of ENSO phases and data pertaining to frequency of named storms, mean number of named storms per year, and the mean annual rainfall, comparing between ENSO phases.

ENSO	Frequency	No. Named Storms	Mean no. Storms/year	Mean Annual Precipitation (mm)
El Niño	5	2	0.40	828.2 (n=3)
La Niña	10	18	1.80	997.2 (n=7)
Neutral	14	10	0.71	965.0 (n=12)

Table S10. Likelihood of lahars under a range of antecedent conditions. Likelihood has been calculated via the ratio of days with observed lahars vs days with no lahars. The first row 'All conditions' considers the likelihood of a lahar regardless of the antecedent conditions. High and Low sediment availability has been determined from observations of valley fill or erosion, respectively, in the upper catchment. High to Low vegetation cover has been determined arbitrarily according to the percentage cover of vegetation/bare surface. Low, Medium, and High antecedent rainfall are defined as the mean antecedent rainfall and below, between the mean and one standard deviation above the mean, and above one standard deviation, respectively. Entries of zero indicate where rainfall events over given thresholds have been recorded with no associated lahars.

LAHAR LIKELIHOOD (%)		**Rainfall threshold**												
		1-hour max. intensity (mm/hr)							**24-hour total (mm)**					
		>0	**>5**	**>10**	**>20**	**>40**	**>60**	**>80**	**>0**	**>10**	**>20**	**>40**	**>60**	**>80**
	All conditions	4	27	37	45	46	50	66	4	17	22	30	41	40
Sediment availability	High	9	37	46	66	85	100	100	7	26	32	40	58	59
	Low	3	17	23	13	0	0	0	2	8	10	18	24	21
Vegetation	High (>85%)	3	24	38	48	50	0	0	3	15	19	30	39	41
	Medium (65-85%)	4	30	36	33	16	50	100	4	16	20	26	30	27
	Low (<65%)	9	36	43	62	100	100	100	7	30	37	45	77	78
Antecedent rainfall (3-day)	High	10	40	48	63	50	50	100	10	31	37	50	58	50
	Medium	5	32	34	25	50	0	0	6	22	29	43	60	55
	Low	3	21	34	42	40	100	100	3	20	27	43	55	66
Antecedent rainfall (7-day)	High	9	47	66	72	60	50	100	9	40	51	54	63	56
	Medium	6	36	38	14	0	0	0	6	26	28	47	55	50
	Low	3	18	26	40	66	100	100	3	16	22	38	55	64

Supplementary Code

Below is the code used to access Landsat data via Google Earth Engine. Please note that some parts of this code may have since depreciated and will need to be edited prior to use.

```
// Acquisition of monthly median NDVI geotifs and
// values for Montserrat.
//
// NB errors of the nature 'Pattern 'NDVI' did not match
// any bands' are expected, and will occur for all years
// bar 2013 (when both L7 and L8 imagery is present).
//
// Author: Tom Chudley
// Thomas.r.chudley@durham.ac.uk | Durham University
// based on http://www.timassal.com/?tag=ndvi-time-series


// Define input variables
// (Included values are examples)

var year = 2006;
var startmonth = 1, endmonth = 4;
// var belham already imported from asset bank

// Filter Landsat collections

var l5collection = ee.ImageCollection('LANDSAT/LT05/C01/T1_SR')
 .filterBounds(belham)
 .filter(ee.Filter.calendarRange(year,year, 'year'))
 .filter(ee.Filter.calendarRange(startmonth,endmonth,'month'))
 .sort('date');

var l7collection = ee.ImageCollection('LANDSAT/LE07/C01/T1_SR')
 .filterBounds(belham)
 .filter(ee.Filter.calendarRange(year,year, 'year'))
 .filter(ee.Filter.calendarRange(startmonth,endmonth,'month'))
 .sort('date');

var l8collection = ee.ImageCollection('LANDSAT/LC08/C01/T1_SR')
 .filterBounds(belham)
 .filter(ee.Filter.calendarRange(year,year, 'year'))
 .filter(ee.Filter.calendarRange(startmonth,endmonth,'month'))
 .sort('date');
```

```
print(l5collection)
print(l7collection)
print(l8collection)


// Mask pixels with clouds and cloud shadows using the 'pixel_qa' band.
// Modified function from GEE documentation -- also clips to Monteserrat boundary

var cloudMask = function(image) {
  // crop to Monteserrat/belham
  var image = image.clip(bhmsq)
  // If the cloud bit (5) is set and the cloud confidence (7) is high
  // or the cloud shadow bit is set (3), then it's a bad pixel.
  var qa = image.select('pixel_qa');

  var cloud = qa.bitwiseAnd(1 << 5)
              .and(qa.bitwiseAnd(1 << 7))
              .or(qa.bitwiseAnd(1 << 3));

  var land = qa.bitwiseAnd(1 << 0) // alternative masking experiment to solve the 2016 issue - unused
for now
             .or(qa.bitwiseAnd(1 << 1))

  // Remove edge pixels that don't occur in all bands
  var mask2 = image.mask().reduce(ee.Reducer.min());
  return image.updateMask(cloud.not()) // land) //
            .updateMask(mask2);
};

var l8masked = l8collection.map(cloudMask);
var l7masked = l7collection.map(cloudMask);
var l5masked = l5collection.map(cloudMask);

// Get NDVI using NIR (L8: B5, L7/L5: B4) and the red band (L8: B4, L7/L5: B3)

var getNDVI_l8 = function(img){
  return img.addBands(img.normalizedDifference(['B5','B4']).rename('NDVI'));
};
var getNDVI_l7 = function(img){
  return img.addBands(img.normalizedDifference(['B4','B3']).rename('NDVI'));
};
var getNDVI_l5 = function(img){
  return img.addBands(img.normalizedDifference(['B4','B3']).rename('NDVI'));
};

var l8ndvi = l8masked.map(getNDVI_l8);
```

```
var l7ndvi = l7masked.map(getNDVI_l7);
var l5ndvi = l5masked.map(getNDVI_l5);

// Create median composite

var l8composite = l8ndvi.select(['B4', 'B3', 'B2', 'NDVI'], ['red', 'green', 'blue', 'NDVI'])
                  .median()//.qualityMosaic('NDVI')

var l7composite = l7ndvi.select(['B3', 'B2', 'B1', 'NDVI'], ['red', 'green', 'blue', 'NDVI'])
                  .median()//.qualityMosaic('NDVI')

var l5composite = l5ndvi.select(['B3', 'B2', 'B1', 'NDVI'], ['red', 'green', 'blue', 'NDVI'])
                  .median()//.qualityMosaic('NDVI')


// Visualise on map

var visParams = {min: 0, max: 2000, bands: ['red', 'green', 'blue']};
Map.addLayer(l8composite, visParams, 'Visible image L8');
Map.addLayer(l7composite, visParams, 'Visible image L7');
Map.addLayer(l5composite, visParams, 'Visible image L5');

var ndviParams = {min: 0, max: 1, palette: ['brown', 'yellow', 'green']};
Map.addLayer(l8composite.select('NDVI'), ndviParams, 'NDVI image L8');
Map.addLayer(l7composite.select('NDVI'), ndviParams, 'NDVI image L7');
Map.addLayer(l5composite.select('NDVI'), ndviParams, 'NDVI image L5');


Map.centerObject(bhmsq)


// Export to Drive -- NB only bother exporting the satellite that has
// data for a given year, based on the visible layers.

var string = year.toString(10).concat('_', startmonth.toString(10), '_', endmonth.toString(10) )

Export.image.toDrive({
  image: l5composite.select(['red', 'green', 'blue']),      // image to export
  description: 'Ortho_'.concat(string, '_L5'),
  folder: 'Google Earth Engine Assets',
  fileNamePrefix: 'Ortho_'.concat(string, '_L5'),
  scale: 30,              // Resolution in m/pixel
  maxPixels: 1e12,        // Effectively no limit to max pixels
  region: belham,         // Output geometry matches input DEM
  skipEmptyTiles: true,   // Skip empty image tiles
});
```

```
Export.image.toDrive({
  image: l5composite.select(['NDVI']),       // image to export
  description: 'NDVI_'.concat(string, '_L5'),
  folder: 'Google Earth Engine Assets',
  fileNamePrefix: 'NDVI_'.concat(string, '_L5'),
  scale: 30,              // Resolution in m/pixel
  maxPixels: 1e12,        // Effectively no limit to max pixels
  region: belham,       // Output geometry matches input DEM
  skipEmptyTiles: true,    // Skip empty image tiles
});

Export.image.toDrive({
  image: l7composite.select(['red', 'green', 'blue']),       // image to export
  description: 'Ortho_'.concat(string, '_L7'),
  folder: 'Google Earth Engine Assets',
  fileNamePrefix: 'Ortho_'.concat(string, '_L7'),
  scale: 30,              // Resolution in m/pixel
  maxPixels: 1e12,        // Effectively no limit to max pixels
  region: belham,       // Output geometry matches input DEM
  skipEmptyTiles: true,    // Skip empty image tiles
});

Export.image.toDrive({
  image: l7composite.select(['NDVI']),       // image to export
  description: 'NDVI_'.concat(string, '_L7'),
  folder: 'Google Earth Engine Assets',
  fileNamePrefix: 'NDVI_'.concat(string, '_L7'),
  scale: 30,              // Resolution in m/pixel
  maxPixels: 1e12,        // Effectively no limit to max pixels
  region: belham,       // Output geometry matches input DEM
  skipEmptyTiles: true,    // Skip empty image tiles
});

Export.image.toDrive({
  image: l8composite.select(['red', 'green', 'blue']),       // image to export
  description: 'Ortho_'.concat(string, '_L8'),
  folder: 'Google Earth Engine Assets',
  fileNamePrefix: 'Ortho_'.concat(string, '_L8'),
  scale: 30,              // Resolution in m/pixel
  maxPixels: 1e12,        // Effectively no limit to max pixels
  region: belham,       // Output geometry matches input DEM
  skipEmptyTiles: true,    // Skip empty image tiles
});

Export.image.toDrive({
```

```
  image: l8composite.select(['NDVI']),       // image to export
  description: 'NDVI_'.concat(string, '_L8'),
  folder: 'Google Earth Engine Assets',
  fileNamePrefix: 'NDVI_'.concat(string, '_L8'),
  scale: 30,              // Resolution in m/pixel
  maxPixels: 1e12,         // Effectively no limit to max pixels
  region: belham,        // Output geometry matches input DEM
  skipEmptyTiles: true,    // Skip empty image tiles
});
```

References

Akca, D. (2010). Co-registration of surfaces by 3D least squares matching. *Photogrammetric Engineering & Remote Sensing*, *76*(3), 307–318. https://doi.org/10.14358/PERS.76.3.307

Alexander, J., Barclay, J., Sušnik, J., Loughlin, S. C., Herd, R. A., Darnell, A., & Crosweller, S. (2010). Sediment-charged flash floods on Montserrat: The influence of synchronous tephra fall and varying extent of vegetation damage. *Journal of Volcanology and Geothermal Research*, *194*(4), Article 4. https://doi.org/10.1016/j.jvolgeores.2010.05.002

Barclay, J., Alexander, J., & Sušnik, J. (2007). Rainfall-induced lahars in the Belham valley, Montserrat, West Indies. *Journal of the Geological Society*, *164*(4), Article 4.

Bertin, S., Jaud, M., & Delacourt, C. (2022). Assessing DEM quality and minimizing registration error in repeated geomorphic surveys with multi-temporal ground truths of invariant features: Application to a long-term dataset of beach topography and nearshore bathymetry. *Earth Surface Processes and Landforms*, *47*(12), 2950–2971. https://doi.org/10.1002/esp.5436

Bisson, M., Spinetti, C., Andronico, D., Palaseanu-Lovejoy, M., Buongiorno, M. F., Alexandrov, O., & Cecere, T. (2021). Ten years of volcanic activity at Mt Etna: High-resolution mapping and accurate quantification of the morphological changes by Pleiades and Lidar data. *International Journal of Applied Earth Observation and Geoinformation*, *102*, 102369. https://doi.org/10.1016/j.jag.2021.102369

Buma, B. (2012). Evaluating the utility and seasonality of NDVI values for assessing post-disturbance recovery in a subalpine forest. *Environmental Monitoring and Assessment*, *184*(6), Article 6. https://doi.org/10.1007/s10661-011-2228-y

Burt, T. P., & Allison, R. J. (2010). Sediment Cascades in the Environment: An Integrated Approach. In T. P. Burt & R. J. Allison (Eds.), *Sediment Cascades* (1st ed., pp. 1–15). Wiley. https://doi.org/10.1002/9780470682876.ch1

Calder, E. S., Luckett, R., Sparks, R. S. J., & Voight, B. (2002). Mechanisms of lava dome instability and generation of rockfalls and pyroclastic flows at Soufrière Hills Volcano, Montserrat. *Geological Society, London, Memoirs*, *21*(1), Article 1. https://doi.org/10.1144/GSL.MEM.2002.021.01.08

Carn, S. A., Watts, R. B., Thompson, G., & Norton, G. E. (2004). Anatomy of a lava dome collapse: The 20 March 2000 event at Soufrière Hills Volcano, Montserrat. *Journal of Volcanology and Geothermal Research*, *131*(3), Article 3. https://doi.org/10.1016/S0377-0273(03)00364-0

Chandra, A., Mitra, P., Dubey, S. K., & Ray, S. S. (2019). Machine learning approach for kharif rice yield prediction integrating multi-temporal vegetation indices and weather and non-weather variables. *The International Archives of the Photogrammetry, Remote Sensing and Spatial Information Sciences*, *42*, 187–194. https://doi.org/10.5194/isprs-archives-XLII-3-W6-187-2019

Cole, P. D., Calder, E. S., Druitt, T. H., Hoblitt, R., Robertson, R., Sparks, R. S. J., & Young, S. R. (1998). Pyroclastic flows generated by gravitational instability of the 1996–97 lava dome of Soufriere

Hills Volcano, Montserrat. *Geophysical Research Letters*, *25*(18), Article 18. https://doi.org/10.1029/98GL01510

Cole, P. D., Smith, P. J., Stinton, A. J., Odbert, H. M., Bernstein, M. L., Komorowski, J. C., & Stewart, R. (2014). Chapter 5 Vulcanian explosions at Soufrière Hills Volcano, Montserrat between 2008 and 2010. *Geological Society, London, Memoirs*, *39*(1), Article 1. https://doi.org/10.1144/M39.5

Dai, C., Howat, I. M., Freymueller, J. T., Lu, Z., Vijay, S., Liljedahl, A. K., Ward Jones, M. K., Bergstedt, H., & Lev, E. (2022). Quantifying mass flows at Mt. Cleveland, Alaska between 2001 and 2020 using satellite photogrammetry. *Journal of Volcanology and Geothermal Research*, *429*, 107614. https://doi.org/10.1016/j.jvolgeores.2022.107614

Darnell, A. R. (2010). Application of geographical information systems to lahar hazard assessment on an active volcanic system, *PhD Thesis*, University of East Anglia. https://ueaeprints.uea.ac.uk/id/eprint/47533/

Darnell, A. R., Barclay, J., Herd, R. A., Phillips, J. C., Lovett, A. A., & Cole, P. (2012). Geographical information system approaches for hazard mapping of dilute lahars on Montserrat, West Indies. *Bulletin of Volcanology*, *74*(6), Article 6. https://doi.org/10.1007/s00445-012-0596-y

De Angelis, S., Bass, V., Hards, V., & Ryan, G. (2007). Seismic characterization of pyroclastic flow activity at Soufriere Hills Volcano, Montserrat, 8 January 2007. *Natural Hazards and Earth System Sciences*, *7*(4), 467–472. https://doi.org/10.5194/nhess-7-467-2007

Earth Resources Observation and Science (EROS) Center. (2020a). Landsat 7 Enhanced Thematic Mapper Plus Level-2, Collection 2 [dataset]. *U.S. Geological Survey*. https://doi.org/10.5066/P9C7I13B

Earth Resources Observation and Science (EROS) Center. (2020b). Landsat 8-9 Operational Land Imager / Thermal Infrared Sensor Level-2, Collection 2 [dataset]. *U.S. Geological Survey.* https://doi.org/10.5066/P9OGBGM6.

Finnegan, N. J., Roe, G., Montgomery, D. R., & Hallet, B. (2005). Controls on the channel width of rivers: Implications for modeling fluvial incision of bedrock. *Geology*, *33*(3), 229–232. https://doi.org/10.1130/G21171.1

Froude, M. (2015). Lahar dynamics in the Belham river valley, Montserrat: Application of remote-camera based monitoring for improved sedimentological interpretation of post-event deposits, *PhD Thesis*, University of East Anglia. http://ethos.bl.uk/OrderDetails.do?uin=uk.bl.ethos.656138

Froude, M. J., Alexander, J., Barclay, J., & Cole, P. (2017). Interpreting flash flood palaeoflow parameters from antidunes and gravel lenses: An example from Montserrat, West Indies. *Sedimentology*, *64*(7), 1817–1845. https://doi.org/10.1111/sed.12375

Gran, K. B., & Montgomery, D. R. (2005). Spatial and temporal patterns in fluvial recovery following volcanic eruptions: Channel response to basin-wide sediment loading at Mount Pinatubo, Philippines. *GSA Bulletin*, *117*(1–2), Article 1–2. https://doi.org/10.1130/B25528.1

Gran, K. B., Montgomery, D. R., & Halbur, J. C. (2011). Long-term elevated post-eruption sedimentation at Mount Pinatubo, Philippines. *Geology*, *39*(4), Article 4. https://doi.org/10.1130/G31682.1

Hall, F. G., Hilker, T., & Coops, N. C. (2012). Data assimilation of photosynthetic light-use efficiency using multi-angular satellite data: I. Model formulation. *Remote Sensing of Environment*, *121*, 301–308. https://doi.org/10.1016/j.rse.2012.02.007

Herd, R. A., Edmonds, M., & Bass, V. A. (2005). Catastrophic lava dome failure at Soufrière Hills volcano, Montserrat, 12–13 July 2003. *Journal of Volcanology and Geothermal Research*, *148*(3–4), Article 3–4. https://doi.org/10.1016/j.jvolgeores.2005.05.003

Hodúl, M., Bird, S., Knudby, A., & Chénier, R. (2018). Satellite derived photogrammetric bathymetry. *ISPRS Journal of Photogrammetry and Remote Sensing*, *142*, 268–277. https://doi.org/10.1016/j.isprsjprs.2018.06.015

Johnson, J. B., Roca, A., Pineda, A., Mérida, R., Escobar-Wolf, R., Anderson, J. F., Mock, J., Bosa, A., Bejar, G., & P. Waite, G. (2023). Infrasound detection of approaching lahars. *Scientific Reports*, *13*(1), 6476. https://doi.org/10.1038/s41598-023-32109-2

Lai, R., Oguchi, T., & Zhong, C. (2022). Evaluating Spatiotemporal Patterns of Post-Eruption Vegetation Recovery at Unzen Volcano, Japan, from Landsat Time Series. *Remote Sensing*, *14*(21), 5419. https://doi.org/10.3390/rs14215419

Lavigne, F. (2004). Rate of sediment yield following small-scale volcanic eruptions: A quantitative assessment at the Merapi and Semeru stratovolcanoes, Java, Indonesia. *Earth Surface Processes and Landforms*, *29*(8), Article 8. https://doi.org/10.1002/esp.1092

Lillo, D. L., Delgado, F., Pritchard, M., Ruprecht, P., & Muñoz-Saez, C. (2024). Multiple sources of elevation change during and after the 2011–2012 Cordón Caulle, Chile eruption measured by satellite topographic time series. *Volcanica*, *7*(2), 541–564. https://doi.org/10.30909/vol.07.02.541564

Lindsay, E., Frauenfelder, R., Rüther, D., Nava, L., Rubensdotter, L., Strout, J., & Nordal, S. (2022). Multi-temporal satellite image composites in google earth engine for improved landslide visibility: A case study of a glacial landscape. *Remote Sensing*, *14*(10), 2301. https://doi.org/10.3390/rs14102301

Major, J. J., Mosbrucker, A. R., & Spicer, K. R. (2018). Sediment erosion and delivery from Toutle River basin after the 1980 eruption of Mount St. Helens: A 30-year perspective. In *Ecological Responses at Mount St. Helens: Revisited 35 years after the 1980 Eruption* (pp. 19–44). Springer. https://doi.org/10.1007/978-1-4939-7451-1_2

Major, J. J., Spicer, K. R., & Mosbrucker, A. R. (2021). Effective hydrological events in an evolving mid-latitude mountain river system following cataclysmic disturbance—A saga of multiple influences. *Water Resources Research*, https://doi.org/10.1029/2019WR026851

Mancini, F., & Salvini, R. (2019). Applications of photogrammetry for environmental research. In *ISPRS International Journal of Geo-Information* (Vol. 8, Issue 12, p. 542). MDPI. https://www.mdpi.com/2220-9964/8/12/542/htm

NASA/METI/AIST/Japan Spacesystems and U.S./Japan ASTER Science Team. (n.d.). ASTER Level 2 Surface Reflectance Product. *NASA EOSDIS Land Processes Distributed Active Archive Center*. https://doi.org/10.5067/ASTER/AST_07.003

Planet Labs PBC. (2022). *Planet Application Program Interface: In Space for Life on Earth*. https://api.planet.com

Pierson, T. C., Pringle, P. T., & Cameron, K. A. (2011). Magnitude and timing of downstream channel aggradation and degradation in response to a dome-building eruption at Mount Hood, Oregon. *GSA Bulletin*, *123*(1–2), Article 1–2. https://doi.org/10.1130/B30127.1

Pierson, T. C., & Major, J. J. (2014). Hydrogeomorphic effects of explosive volcanic eruptions on drainage basins. *Annual Review of Earth and Planetary Sciences*, *42*. https://doi.org/10.1146/annurev-earth-060313-054913

Rivas-Torres, G. F., Benítez, F. L., Rueda, D., Sevilla, C., & Mena, C. F. (2018). A methodology for mapping native and invasive vegetation coverage in archipelagos: An example from the Galápagos Islands. *Progress in Physical Geography: Earth and Environment*, *42*(1), Article 1. https://doi.org/10.1177/0309133317752278

Rodgers, J. C., Murrah, A. W., & Cooke, W. H. (2009). The Impact of Hurricane Katrina on the Coastal Vegetation of the Weeks Bay Reserve, Alabama from NDVI Data. *Estuaries and Coasts*, *32*(3), Article 3. https://doi.org/10.1007/s12237-009-9138-z

Shelestov, A., Lavreniuk, M., Kussul, N., Novikov, A., & Skakun, S. (2017). Exploring Google Earth Engine platform for big data processing: Classification of multi-temporal satellite imagery for crop mapping. *Frontiers in Earth Science*, *5*, 232994. https://doi.org/10.3389/feart.2017.00017

Sotille, M. E., Bremer, U. F., Vieira, G., Velho, L. F., Petsch, C., & Simões, J. C. (2020). Evaluation of UAV and satellite-derived NDVI to map maritime Antarctic vegetation. *Applied Geography*, *125*, 102322. https://doi.org/10.1016/j.apgeog.2020.102322

Sparks, R. S. J., & Young, S. R. (2002). The eruption of Soufrière Hills Volcano, Montserrat (1995-1999): Overview of scientific results. *Geological Society, London, Memoirs*, *21*(1), Article 1. https://doi.org/10.1144/GSL.MEM.2002.021.01.03

Stinton, A. J., Cole, P. D., Odbert, H. M., Christopher, T., Avard, G., & Bernstein, M. (2014a). Chapter 6 Dome growth and valley fill during Phase 5 (8 October 2009–11 February 2010) at the Soufrière Hills Volcano, Montserrat. *Geological Society, London, Memoirs*, *39*(1), Article 1. https://doi.org/10.1144/M39.6

Stinton, A. J., Cole, P. D., Stewart, R. C., Odbert, H. M., & Smith, P. (2014b). Chapter 7 The 11 February 2010 partial dome collapse at Soufrière Hills Volcano, Montserrat. *Geological Society, London, Memoirs*, *39*(1), Article 1. https://doi.org/10.1144/M39.7

Stumpf, A., Michéa, D., & Malet, J.-P. (2017). Generation of Digital Surface Models from satellite photogrammetry: The DSM-OPT service of the ESA Geohazards Exploitation Platform (GEP). 4481. *EGU General Assembly Conference Abstracts*.

Susnik, J. (2008). Lahars in the Belham River Valley, Montserrat, West Indies, *PhD Thesis*, University of East Anglia.

Sutton, S. S., Richardson, J. A., Whelley, P. L., Scheidt, S. P., & Hamilton, C. W. (2024). Degradation of the 2014–2015 Holuhraun vent-proximal edifice in Iceland. *Bulletin of Volcanology*, *86*(4), 37. https://doi.org/10.1007/s00445-024-01709-9

Tang, L., He, M., & Li, X. (2020). Verification of fractional vegetation coverage and NDVI of desert vegetation via UAVRS technology. *Remote Sensing*, *12*(11), 1742. https://doi.org/10.3390/rs12111742

Thapa, S., Garcia Millan, V. E., & Eklundh, L. (2021). Assessing forest phenology: A multi-scale comparison of near-surface (UAV, spectral reflectance sensor, phenocam) and satellite (MODIS, sentinel-2) remote sensing. *Remote Sensing*, *13*(8), 1597. https://doi.org/10.3390/rs13081597

Thouret, J.-C., Oehler, J.-F., Gupta, A., Solikhin, A., & Procter, J. N. (2014). Erosion and aggradation on persistently active volcanoes—A case study from Semeru Volcano, Indonesia. *Bulletin of Volcanology*, *76*(10), Article 10. https://doi.org/10.1007/s00445-014-0857-z

Valderrama-Landeros, L., Flores-de-Santiago, F., Kovacs, J. M., & Flores-Verdugo, F. (2017). An assessment of commonly employed satellite-based remote sensors for mapping mangrove species in Mexico using an NDVI-based classification scheme. *Environmental Monitoring and Assessment*, *190*(1), Article 1. https://doi.org/10.1007/s10661-017-6399-z

Vallejo, S., Diefenbach, A. K., Gaunt, H. E., Almeida, M., Ramón, P., Naranjo, F., & Kelfoun, K. (2024). Twenty years of explosive-effusive activity at El Reventador volcano (Ecuador) recorded in its geomorphology. *Frontiers in Earth Science*, *11*, 1202285. https://doi.org/10.3389/feart.2023.1202285

Walk, J., Stauch, G., Bartz, M., Brückner, H., & Lehmkuhl, F. (2019). Geomorphology of the coastal alluvial fan complex Guanillos, northern Chile. *Journal of Maps*, *15*(2), 436–447. https://doi.org/10.1080/17445647.2019.1611499

Wadge, G. (2000). A DEM of the volcanic deposits of Soufrière Hills Volcano during 1999. *Open File Report 00-07-1999,* Montserrat Volcano Observatory.

Waythomas, C. F., Scott, W. E., & Nye, C. J. (2010). The Geomorphology of an Aleutian Volcano following a Major Eruption: The 7–8 August 2008 Eruption of Kasatochi Volcano, Alaska, and Its Aftermath. *Arctic, Antarctic, and Alpine Research*, *42*(3), Article 3. https://doi.org/10.1657/1938-4246-42.3.260

Westoby, M. J., Brasington, J., Glasser, N. F., Hambrey, M. J., & Reynolds, J. M. (2012). 'Structure-from-Motion' photogrammetry: A low-cost, effective tool for geoscience applications. *Geomorphology*, *179*, 300–314. https://doi.org/10.1016/j.geomorph.2012.08.021

Yan, L., & Roy, D. P. (2014). Automated crop field extraction from multi-temporal Web Enabled Landsat Data. *Remote Sensing of Environment*, *144*, 42–64. https://doi.org/10.1016/j.rse.2014.01.006

Zobin, V. M. (2022). Volcano Seismology: An Introduction. In R. I. Tilling (Ed.), *Complexity in Tsunamis, Volcanoes, and their Hazards* (pp. 393–424). Springer US. https://doi.org/10.1007/978-1-0716-1705-2_607